



# Paradox of thiourea: A false-positive and promoter for electrochemical nitrogen reduction on nickel sulfide catalysts

Min-Cheol Kim<sup>a,b,1</sup>, Jiyong Chung<sup>c,d,1</sup>, Tae-Yong An<sup>e,1</sup>, Jaeyoung Lee<sup>c,1</sup>, Mi-Kyung Han<sup>f</sup>, Shinbi Lee<sup>g</sup>, Wonyong Choi<sup>g</sup>, Jung Kyu Kim<sup>g</sup>, Sang Soo Han<sup>a,\*</sup>, Uk Sim<sup>e,h,\*\*</sup>, Taekyung Yu<sup>c,\*</sup>

<sup>a</sup> Computational Science Research Center, Korea Institute of Science and Technology, Seoul 02792, Republic of Korea

<sup>b</sup> School of Chemical Engineering, Sungkyunkwan University, Suwon 16419, Republic of Korea

<sup>c</sup> Department of Chemical Engineering, College of Engineering, Integrated Engineering Major, Kyung Hee University, Yongin 17104, Republic of Korea

<sup>d</sup> G. W. Woodruff School of Mechanical Engineering, Georgia Institute of Technology, Atlanta, GA 30332, USA

<sup>e</sup> School of Energy Technology, Korea Institute of Energy Technology (KENTECH), Jeollanamdo 58330, Republic of Korea

<sup>f</sup> Department of Materials Science & Engineering, Chonnam National University, Gwangju 61186, Republic of Korea

<sup>g</sup> KENTECH Institute for Environmental and Climate Technology, Korea Institute of Energy Technology (KENTECH), Naju 58330, Republic of Korea

<sup>h</sup> Research Institute, NEEL Sciences, INC., Gwangju 61186, Republic of Korea

## ARTICLE INFO

### Keywords:

Electrochemical ammonia production

Nitrogen reduction reaction

Thiourea

Nickel sulfide

Carbon doping

## ABSTRACT

Electrochemical nitrogen reduction reaction (NRR) is an environmentally friendly process for ammonia synthesis. An unusually high  $\text{NH}_3$  production rate ( $86.91 \pm 9.29 \mu\text{g h}^{-1} \text{cm}^{-2}$ ) and Faradaic efficiency (F.E.) ( $57.17 \pm 4.14\%$ ) was observed in electrochemical tests on NiS catalysts synthesized using thiourea (TU). Through joint experiment-theory work, we demonstrate the paradoxical catalytic effect of TU as a false positive from TU-derived thiocyanate reduction and a promoter via the generation of catalytically active carbon sites after TU reduction on the NiS surface (with an effective  $\text{NH}_3$  rate of  $52 \pm 5.57 \mu\text{g h}^{-1} \text{cm}^{-2}$ ). TU reduction leads to the substitution of an S atom to a reactive C atom with fewer valence electrons, facilitating a more facile NRR pathway. This study presents a new possibility for NRR catalysts based on metal-nonmetal compounds (e.g., sulfides, chalcogenides, or nitrides) by nonmetal dopants with fewer valence electrons to create new catalytically active sites.

## 1. Introduction

Ammonia ( $\text{NH}_3$ ) production from nitrogen reduction is an important chemical reaction due to the vital role of ammonia in food production [1] and hydrogen carriers for fuel cells [2,3]. However, the industrial process for producing ammonia, the Haber-Bosch process, can only be operated under extreme conditions ( $400\text{--}500^\circ\text{C}$  and  $10\text{--}30\text{ MPa}$ ) due to the infamous  $\text{N}_2$  triple bond [4]. Despite the difficulties in achieving a high ammonia production rate and selectivity [5], the electrochemical nitrogen reduction reaction (NRR) under ambient conditions has recently received much interest as an alternative [6–12]. Inspired by the nitrogen fixation enzyme, nitrogenase, and its active site within the Fe-Mo-S cofactor [13,14], the NRR activities of metal sulfide catalysts have recently been explored [15–24]. Furthermore, in a recent

theoretical study, various metal sulfides were proposed as promising candidates for the NRR [25]. In particular, NiS is one of the candidates with promising NRR activity, although the catalyst was predicted to be more selective to the hydrogen evolution reaction (HER) than the NRR [25,26]. Herein, we investigated the NRR activity of NiS in conjunction with cationic HER suppression [27–29] and NRR promotion effects [30] to overcome the predicted low selectivity. During an investigation of the NRR activity of NiS among various electrolytes, we found that NiS with  $\text{Na}_2\text{SO}_4$  electrolytes shows an unusually high ammonia yield of  $86.91 \pm 9.29 \mu\text{g h}^{-1} \text{cm}^{-2}$  and a Faradaic efficiency (F.E.) of  $57.17 \pm 4.14\%$  at an applied potential  $U = -0.4\text{ V}$ . A careful analysis revealed that this superior NRR performance of NiS was contributed by the electrochemical reduction of thiocyanates derived from thiourea, which is a substance used as a sulfur source during NiS synthesis. An ammonia

\* Corresponding authors.

\*\* Corresponding author at: School of Energy Technology, Korea Institute of Energy Technology (KENTECH), Jeollanamdo 58330, Republic of Korea  
E-mail addresses: [sangsoo@kist.re.kr](mailto:sangsoo@kist.re.kr) (S.S. Han), [usim@kentech.ac.kr](mailto:usim@kentech.ac.kr) (U. Sim), [tkyu@khu.ac.kr](mailto:tkyu@khu.ac.kr) (T. Yu).

<sup>1</sup> These authors contributed equally to this work

yield of  $52 \pm 5.57 \mu\text{g h}^{-1} \text{cm}^{-2}$  and an F.E. of  $34.04 \pm 2.48 \%$ , excluding the NRR contribution of thiocyanate reduction, was found from further analysis using Ar control experiments and  $^{15}\text{N}$  isotope experiments. This NRR performance, which is significantly higher than the ammonia yield of  $1.45 \mu\text{g h}^{-1} \text{cm}^{-2}$  and  $6.78 \pm 0.68 \mu\text{g h}^{-1} \text{cm}^{-2}$  from thiourea-deprived NiS catalysts, shows that surface adsorbates can readily act both as false positives and promoters for the NRR. In addition, density functional theory (DFT) calculations elucidate that the thiocyanate reduction process creates activated carbon sites on the NiS surface, where these activated carbon sites enable stronger  $\text{N}_2$  binding and a preferential NRR pathway. We also discuss the possibility of a similar reaction mechanism occurring on thiourea-derived  $\text{MoS}_2$  catalysts with DFT calculations.

## 2. Experimental section

### 2.1. Materials

Thiourea ( $\text{CH}_4\text{N}_2\text{S}$ ,  $\geq 99.0 \%$ ) and sodium sulfide nonahydrate ( $\text{Na}_2\text{S} \cdot 9\text{H}_2\text{O}$ ,  $\geq 99.99 \%$ ) were purchased from Sigma-Aldrich and were used immediately without further purification. Nickel foam (thickness: 1.6 mm) was purchased from Invisible Inc. DI water, ethanol, and hydrochloric acid (HCl, 37 %) were used for pretreatment to remove the oxidized layer on the Ni foam surface. First, the Ni foam ( $0.95 \times 0.95 \text{ cm}^2$ ) was immersed in HCl solution for 30 s. After that, the Ni foam was removed from the HCl solution and moved to a solution composed of DI water and ethanol (volume ratio of 1:1). After sonication, the Ni foam was completely dried at room temperature.

### 2.2. Preparation of NiS catalysts

A total of 10 mL of aqueous thiourea solution (0.3 M) was transferred to a Teflon-lined stainless-steel autoclave (100 mL), and the washed Ni foam ( $0.95 \times 0.95 \text{ cm}^2$ ) was added to the solution. The whole batch was kept at a temperature of  $180^\circ\text{C}$  for 24 h. After the reaction, the foam was washed with DI water and ethanol to remove the remaining residues on the sample surface and dried at room temperature for 6 h.

SS-NiS was prepared under the same experimental conditions as those for TU-NiS, except that the synthesis was conducted using sodium sulfide nonahydrate instead of thiourea. B-NiS was prepared by the process of adding nickel and sulfur powder in a 1:1 molar ratio to a stainless steel reactor. Then, the stainless steel reactor with the mixture and zirconia milling balls (weight ratio 1:9) was sent to a planetary ball milling machine and ball milled at 500 rpm for 12 h.

### 2.3. Surface modification process of NiS catalysts

The surface modification processes were performed to create thiocyanate residues on the surface of SS-NiS and B-NiS. First, surface modification process of SS-NiS was achieved by modifying the existing hydrothermal synthesis method of SS-NiS to use the half amount of sodium sulfide nonahydrate and the half amount of thiourea, instead of only sodium sulfide nonahydrate. Second, surface modification process of B-NiS was carried out by dipping the sample into excess thiourea solution (1 M) at  $80^\circ\text{C}$  for 24 h after the existing synthesis method of B-NiS. After that, it was obtained in the form of powder through a washing process with ethanol and dried in an oven ( $80^\circ\text{C}$ ).

### 2.4. Material characterization

The morphologies of the catalyst surface and the elemental composition were analyzed using scanning electron microscopy (SEM, MERLIN-Carl Zeiss) and an energy dispersive X-ray (EDX) detector, respectively. Powder X-ray diffraction (XRD) measurements were conducted using a Rigaku D/MAX-2200PC X-ray diffractometer with Cu-K $\alpha$  radiation ( $\lambda = 0.154 \text{ nm}$ ) at a scan rate of  $6^\circ/\text{min}$ . The Raman spectra

were obtained using a Horiba Jobin Yvon LabRam Aramis with an Ar-ion laser beam at an exciting radiation wavelength of 514 nm. X-ray photoelectron spectroscopy (XPS) measurements were performed with Nexsa G2 Surface Analysis System (Thermo Fisher Scientific, USA). The Raman spectra were obtained using a Horiba Jobin Yvon LabRam Aramis with an Ar-ion laser beam at an exciting radiation wavelength of 514 nm. Elemental analysis (EA, Flash EA1112, CE) was used to quantify elements such as carbon (C), hydrogen (H), nitrogen (N), and sulfur (S) (accuracy was  $\pm 0.1 \%$  absolute). FT-IR spectra were measured using a JASCO FTIR4700. The spectra were recorded in the range of  $4000\text{--}400 \text{ cm}^{-1}$  at a nominal resolution of  $0.4 \text{ cm}^{-1}$ . The spectrum was corrected based on the air spectrum. Ion chromatography (IC) measurement was performed using IC a Dionex DX-120 equipped with AS-14 column and conductivity detector for anions, with a detection limit of 0.1 nmol. UV-visible spectra were obtained using Evolution Pro One UV-Visible (ThermoFisher Scientific, USA), with photometric accuracy  $\pm 0.004$  (absorbance) and wavelength  $\pm 0.05 \text{ nm}$ .

### 2.5. Electrochemical experiments

The electrochemical NRR activity of the catalysts was evaluated using an H-type cell with a three-electrode system controlled by a workstation (Biologic VSP 200, France). For all electrocatalytic activity experiments, a Hg/HgO electrode and a precleaned Pt spring were employed as the reference and counter electrodes, respectively; a  $\text{Na}_2\text{SO}_4$  solution (50 mL, 0.1 M, pH = 7) served as the electrolyte. A proton exchange membrane (Nafion 117) was used to separate the cathode and anode and was activated by pretreating with 1 M HCl for about 24 h, and then the pretreated membrane was submerged in 0.5 M  $\text{NaSO}_4$  for 1 h to remove traces of additional reactants. The pretreated membranes were involved in all electrochemical measurements. The geometric area of the working electrode was  $0.95 \times 0.95 \text{ cm}^2$ . The potentials reported in this study were converted to the RHE scale by a calibration procedure using the following equation:

$$E(\text{V vs. RHE}) = E(\text{V vs. Hg/HgO}) + 0.118 + 0.059 \times \text{pH}$$

The NRR performance of the catalyst was measured by applied potential electrolysis in an electrolyte for 1 h under ambient conditions (1 atm,  $25^\circ\text{C}$ ). Before each NRR measurement, the electrolyte was saturated with Ar (99.999 %),  $^{14}\text{N}_2$  (99.999 %), and  $^{15}\text{N}_2$  (98 %) at  $5 \text{ mL min}^{-1}$  for 30 min and a gas-tight state was maintained. For each electrochemical measurement, the used electrodes were replaced by fresh ones to authenticate the electrocatalytic activity. The Ar,  $^{14}\text{N}_2$  and  $^{15}\text{N}_2$  utilized in the experiments were purified using 0.5 M  $\text{H}_2\text{SO}_4$  and 0.1 M KOH  $\text{NO}_x$  scrubber to eliminate interference from nitrogen compounds ( $\text{NH}_3$ , NO,  $\text{NO}_2$ , and  $\text{NO}_3$ ) following the procedure of Choi et al. [31] (Fig. S1). A Dionex aquion ion chromatography system (Thermo Fischer Scientific, USA) was used to measure the concentration of  $\text{NO}_x$  ions before and after purification (Figs. S2–3).  $\text{NO}_2^-$  was undetectable up to the detection limit and a marginal amount (22–22 nmol) of  $\text{NO}_3^-$  was detected.

### 2.6. Quantification of ammonia

The produced ammonia was measured using a colorimetric indophenol blue method for three separate experiments with different catalyst samples. The presented ammonia production rate is the average rate of three different experiments. First, 2 mL of electrolyte was collected from the sample after the chronoamperometry test was completed. Then, 1.25 mL of solution containing 0.625 M NaOH, 0.36 M salicylic acid and 0.17 M sodium citrate was added; next, 150  $\mu\text{L}$  sodium nitroferricyanide solution ( $10 \text{ mg mL}^{-1}$ ) and 75  $\mu\text{L}$  NaClO solution were added. A reactant with blue light was then produced after holding the sample at  $25^\circ\text{C}$  for 30 min, and the concentration of  $\text{NH}_3$  in the electrolyte was determined using the absorbance of UV-vis at a wavelength

of 680 nm. The ammonium absorbance curve concentration was calibrated using standard  $\text{NH}_4\text{Cl}$  with a 0.1 M  $\text{NaSO}_4$  electrolyte and a series of  $\text{NH}_3/\text{NH}_4^+$  concentrations (0, 0.94, 1.88, 3.75, and  $7.5 \mu\text{g mL}^{-1}$ ). The fitting curve ( $y = 0.162x - 0.009$ ,  $R^2 = 0.996$ ) shows a linear relationship between the absorbance and ammonia concentration. The electrochemical cell was stabilized at open circuit voltage (OCV) under Ar saturation for 10 min prior to the chronopotentiometry tests measured at an applied current density of  $-1 \text{ mA/cm}^2$ . The cyclic stability tests were performed in Ar and  $\text{N}_2$  saturated conditions at a fixed potential of  $-0.4 \text{ V}$  (vs. RHE). Prior to the cyclic stability test the negligible impurities in the source gas were removed by using an acid trap connected to the system.

## 2.7. Isotope labeling test

The  $^{15}\text{NRR}$  was carried out using the abovementioned conditions with  $^{15}\text{N}_2$  gas. First, the electrolyte was acidified to pH 3 by the addition of 0.5 M  $\text{H}_2\text{SO}_4$ , and then 50 mL of the electrolyte was vacuum distilled at  $70^\circ\text{C}$  and concentrated to 5 mL. Then, for NMR measurement, 0.6 mL of the concentrated solution and 0.06 mL of  $\text{D}_2\text{O}$  (Sigma-Aldrich, 99.99 %) were mixed, and  $^1\text{H}$  NMR analysis was performed (Bruker Avance III 400 MHz).  $^1\text{H}$  NMR was performed spectral width of  $\sim 9.0 \text{ ppm}$  and a resolution of 0.12 Hz (1 ppm is equal to 400 cycles / 1 s), with a resolution of 0.25  $\mu\text{g/mL}$  ammonium ion. The estimated ammonia production rate is the average rate of three different experiments.

## 2.8. Determination of yield and Faradaic efficiency

The yield rate of  $\text{NH}_3$  ( $R_{\text{NH}_4}$ ) was calculated as follows:

$$R_{\text{NH}_4} = [\text{NH}_4^+] \times V / (A_{\text{cat}} \times t)$$

FE was calculated based on the charge consumed for NRR and the total charge passed through the electrode, as follows:

$$\text{FE}(\%) = 3 \times F \times [\text{NH}_4^+] \times V / (18 \times |Q|) \times 100\%$$

where  $[\text{NH}_4^+]$  is the measured concentration of  $\text{NH}_3$  ( $\mu\text{g mL}^{-1}$ ) in the electrolyte,  $V$  is the electrolyte volume,  $A_{\text{cat}}$  is the area of the catalyst ( $0.95 \times 0.95 \text{ cm}^2$ ),  $t$  is the electrolysis time,  $F$  is the Faraday constant ( $96485 \text{ C mol}^{-1}$ ), and  $Q$  is the total charge passed through the electrode.

## 2.9. First-principles calculations

All of the first-principles density functional theory (DFT) calculations were performed using the Vienna *Ab Initio* Simulation Package (VASP) [32] with the revised Perdew–Burke–Ernzerhof (RPBE) [33] functional as the exchange and correlation functional with the D3 dispersion correction [34]. The projector-augmented-wave method was adopted to describe the potential from the ionic core [35], and an energy cutoff of 500 eV was used. Monkhorst-Pack  $k$ -point sampling with  $k$ -point spacing  $< 0.03 \text{ \AA}^{-1}$  was used for all systems. Spin polarization and dipole correction were also included.

We adopted the most stable surface of rhombohedral NiS ( $\beta$ -NiS) from the literature [36], which is the S-terminated (110) slab structure with a cell size of  $10.9 \text{ \AA} \times 9.4 \text{ \AA} \times 22.9 \text{ \AA}$  with a vacuum of  $15 \text{ \AA}$  in  $z$  direction (Fig. S4). Since the B-NiS catalyst has a mixed phase of  $\alpha$ -NiS and  $\beta$ -NiS, we also constructed a hexagonal  $\alpha$ -NiS (001) surface with a cell size of  $10.3 \text{ \AA} \times 10.3 \text{ \AA} \times 24.0 \text{ \AA}$  with a vacuum of  $15 \text{ \AA}$  in  $z$  direction, where the (001) surface is the most closed-packed surface for hcp crystals. The top half of the slab model and the adsorbates were allowed to relax until the forces on the individual relaxed atoms were less than  $0.03 \text{ eV \AA}^{-1}$  and  $0.05 \text{ eV \AA}^{-1}$  for vacuum and explicit solvent calculations, respectively, while the bottom half of the slab model was fixed during the optimization process.

To calculate the Gibbs free energy change of each elementary, the potential under standard reaction conditions (298 K and 1 atm) was set

as the reference potential, in which the chemical potential of the ( $\text{H}^+ + e^-$ ) pair was related to half of the chemical potential of a hydrogen gas molecule ( $\text{H}_2$ ) at pH 0 [37]. For each step,  $\Delta G = \Delta H + T\Delta S + \Delta E_{\text{ZPE}} + \Delta G_U$ . Here, the enthalpy  $H = E + E_{\text{ZPE}} + \int_0^T C_V dT$ , where  $E$  is the electronic energy,  $E_{\text{ZPE}}$  is the zero-point correction energy, and the last term is the integration of heat capacity.  $T$  is the absolute temperature and  $S$  is the entropy.  $E_{\text{ZPE}}$ ,  $\int_0^T C_V dT$ , and  $S$  can all be derived from vibrational frequencies of adsorbed species, which are evaluated from finite difference calculations. We adopted the free energy corrections of the reference gas molecules ( $\text{N}_2$ ,  $\text{H}_2$ , and  $\text{NH}_3$ ) from experimental data [38].  $\Delta G_U$  represents the effect of applied bias and is equal to  $-neU$ , where  $n$  is the number of transferred electrons in each step. We verified that the solvation effects on the Gibbs free energy difference were marginal ( $< 0.1 \text{ eV}$ ) on a test case of the  $^*\text{N}_2$  adsorption structure on the  $^*\text{C}$ -NiS slab, where the solvation energy was evaluated with implicit water solvents within the VASPsol package [39]. The climbing-image nudged elastic band (CI-NEB) method was employed for transition state (TS) calculations [40]. To determine the initial structure for explicit MA solvent molecules, we performed an ab initio molecular dynamics simulation for 5 ps (picoseconds) at 298.15 K on the (110)  $\beta$ -NiS  $^*\text{C}$  site slab model with  $20 \text{ \AA}$  thickness of ice-like water molecules filled inside the simulation cell. The number of water molecules were determined to maintain the density of water at 298.15 K. After equilibration, we took a snapshot from the trajectory and removed all MA molecules except the lowest layer of 6 water molecules.

## 3. Results and discussion

### 3.1. Synthesis and characterization

We prepared three types of NiS electrodes as follows: TU-NiS, for which the sulfur source is from thiourea, B-NiS, which is prepared by ball milling, and SS-NiS, for which the sulfur source is from  $\text{Na}_2\text{S}$  (Fig. 1a-c, S5a-b, and S6a-b). From the X-ray diffraction (XRD) patterns, the crystal structure of the NiS electrodes was confirmed to be TU-NiS: rhombohedral  $\beta$ -NiS, B-NiS: rhombohedral  $\beta$ -NiS + hexagonal  $\alpha$ -NiS, and SS-NiS: trigonal  $\text{Ni}_3\text{S}_2$ , respectively (Fig. 1d, S5c, and S6c). The Raman spectra and FT-IR spectra of the NiS electrodes show that there are thiocyanate-related bindings on the surfaces of the TU-NiS electrodes, while such peaks are not observed for the FT-IR spectra of B-NiS (Fig. 1e-f and Fig. S7). The surface thiocyanate species can be explained by the pyrolysis of surface TU groups to thiocyanate groups due to heating process of TU-NiS at  $180^\circ\text{C}$  for 24 h. It is well-known that thiourea can decompose to thiocyanate species at the temperature of  $180$ – $220^\circ\text{C}$  [41,42]. X-ray photoelectron spectroscopy (XPS) results of the as-prepared TU-NiS catalyst also confirms the existence of surface thiocyanated groups on the catalyst (Fig. S8). For the S 2p spectra of the as-prepared TU-NiS catalyst (Fig. S8a), we identified the S 2p<sub>3/2</sub> and S 2p<sub>1/2</sub> peaks for NiS [43,44], and the S 2p<sub>3/2</sub> and S 2p<sub>1/2</sub> peaks of metal-thiocyanate bonding [45]. The marginal peak at 165.9 eV (2.5 % of the total integrated S 2p peak area) is assigned as oxidized S species that can be derived from the oxidized S of the  $[\text{S}=\text{C}-\text{N}]^-$  ion [46], while the peak at 161.2 eV (1.8 % of the total S 2p peak area) corresponds to chemisorbed S on the Ni surface [47]. For the Ni 2p spectra (Fig. S8b), we confirmed Ni 2p<sub>3/2</sub> peaks and 2p<sub>1/2</sub> peaks for NiS [48] and Ni-thiocyanate binding. For the thiocyanate binding, the reported binding energy for Ni–S(CN) binding [49] and Ni–N(C) binding [50] is in similar range, thus either is possible. For the Ni 2p<sub>3/2</sub> peak at 853.9 eV and 2p<sub>1/2</sub> peak at 870.9 eV, we assign the peak to Ni-TU binding peaks. The Ni in Ni-SCN is strongly oxidized, thus has a stronger 2p electron binding energy, compared to the Ni in Ni-TU (Ni-SC(NH<sub>2</sub>)<sub>2</sub>) due to the stronger ionic bonding nature of the Ni-thiocyanate ion pair than the Ni-TU pair [51]. Thiocyanate and TU related bonds are also observed in the C 1s and N 1s XPS spectra (Fig. S8c-d). We identified C 1s peaks for thiocyanate S=C–N bonding [48] and N 1s peaks for SCN–Ni bonding



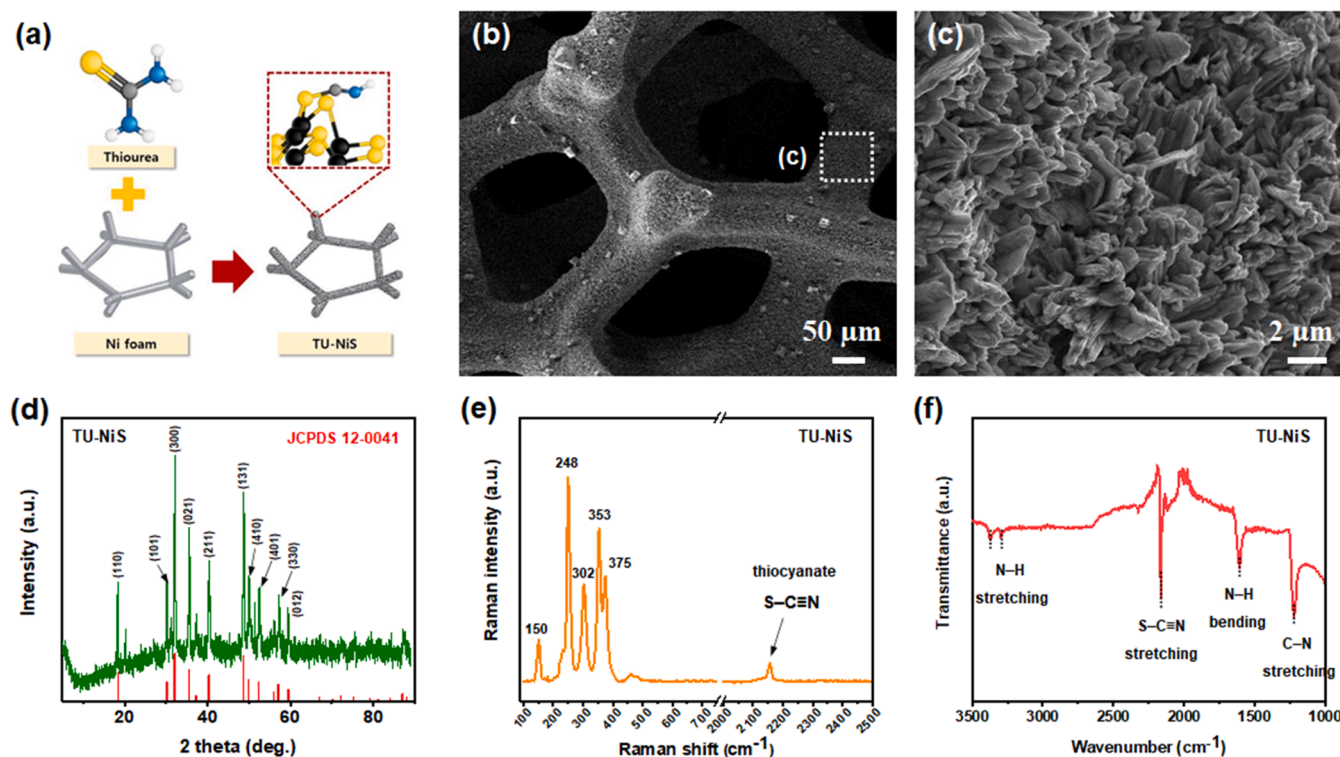


**Fig. 1.** (a) Synthesis scheme of the TU-NiS catalyst. (b) Low- and (c) high-magnification SEM images, (d) XRD patterns, (e) Raman spectra, and (f) FT-IR spectra of TU-NiS.

[48] and TU derived  $\text{-NH}_2$  groups [52].

### 3.2. Catalytic performance of NiS catalysts

Electrochemical measurements were performed on a two-compartment cell (H-cell) at room temperature and atmospheric pressure. Nitrogen ( $^{14}\text{N}$  and  $^{15}\text{N}$ ) and argon were fed during electrolysis, which the current density was measured with the chronoamperometry (CA) (Fig. S9 and S10a-b). The produced ammonia was measured with colorimetric assays using the indophenol blue method and NMR spectra (Fig. 2, S10c-d, and S11–13). To remove any false positives from the impurities of feeding  $^{14}\text{N}$  and  $^{15}\text{N}$  gas, we implemented impurity traps for the feeding gas as suggested in Choi et al.'s work [31] and confirmed only a marginal amount of  $\text{NO}_x$  ion is detected (Figs. S2–3). The concentration of byproducts ( $\text{NO}_2$ ,  $\text{NO}_3$  and  $\text{N}_2\text{H}_4$ ) were cross-checked with colorimetry using the Griess assay method [53] and no byproducts were detected under the detection limit (Fig. S14–15, Table S1). Under the  $\text{N}_2$  environment, TU-NiS exerted an unusually high  $\text{NH}_3$  production rate of  $86.91 \pm 9.29 \mu\text{g h}^{-1} \text{cm}^{-2}$  and an F.E. of  $57.17 \pm 4.14\%$  at  $U = -0.4 \text{ V}$ , while B-NiS under the  $\text{N}_2$  environment showed a relatively low  $\text{NH}_3$  production rate of  $6.40 \pm 0.64 \mu\text{g h}^{-1} \text{cm}^{-2}$  and F.E. of  $32.37 \pm 3.16\%$  at  $U = -0.3 \text{ V}$  (Fig. 2b-c), and SS-NiS also showed a low  $\text{NH}_3$  production rate of  $1.45 \mu\text{g h}^{-1} \text{cm}^{-2}$  and an F.E. of  $2.48\%$  at  $U = -0.4 \text{ V}$  (Fig. S10e) under the  $\text{N}_2$  environment. Fig. 2d shows the UV-vis absorption spectra of electrolytes colored with indophenol indicator after the electrocatalytic reaction in TU-NiS and B-NiS for 1 h at different potentials ranging from  $-0.1 \text{ V}$  to  $-0.6 \text{ V}$  in an Ar atmosphere. Unfortunately, a non-negligible  $\text{NH}_3$  yield ( $34.91 \mu\text{g h}^{-1} \text{cm}^{-2}$ ) was detected for TU-NiS in an Ar environment, in contrast to the marginal  $\text{NH}_3$  production rate of B-NiS (Fig. S13c and Fig. 2e) and SS-NiS (Fig. S10d, Fig. S10f) under an Ar environment. Thus, the high  $\text{NH}_3$  production rate of TU-NiS is most likely a false positive derived from the electrochemical reduction of a substance in the TU-NiS electrode. The surface thiocyanate is the most plausible candidate because thiocyanate was only detected in TU-NiS from the Raman and FT-IR spectra and not detected in B-NiS

(Fig. S7). Our DFT calculation results indeed confirm that the electrochemical reduction of thiocyanate on the TU-NiS surface is feasible with a low overpotential ( $\eta = 0.18 \text{ V}$ ), which explains the relatively high  $\text{NH}_3$  yield even at  $U = -0.1 \text{ V}$  for the TU-NiS catalyst (Fig. S16). The thiourea in the prepared catalyst were controlled by varying its concentration, 0.75, 1.5, 3 mM and their NRR activity were analysed. NRR activity of the thiourea controlled samples were analysed in the  $\text{N}_2$  and Ar atmosphere and the  $\text{NH}_3$  yield were calculated (Fig. 2f). The catalyst in which 0.75 mM thiourea added, showed only marginal difference in the different environments, whereas the catalyst with 1.5 mM thiourea showed better NRR activity in  $\text{N}_2$  than Ar environment. Similarly, the catalyst with 3 mM thiourea displayed the dramatically enhanced yield. On increasing the thiourea content in the catalyst preparation, the active sites of TU-NiS catalyst will increase and result in a better yield.

To investigate the catalytic enhancement in TU-NiS further, we analyzed the  $^1\text{H}$  NMR spectra for TU-NiS after different reaction times (1 h, 5 h, and 10 h) under  $^{15}\text{N}_2$  atmosphere conditions (Fig. 2g). The total amount of ammonia production on TU-NiS increases with the experiment time (Fig. 2h). For TU-NiS, the  $^{15}\text{NH}_3/^{14}\text{NH}_3$  ratio increases with the reaction time, although no  $^{14}\text{NH}_3$  and  $^{15}\text{NH}_3$  signals were detected for B-NiS as shown in Fig. S17. The  $\text{NH}_3$  production rate of the  $\text{N}_2$  experiment is significantly higher than that of the Ar experiment with TU-NiS, implying that the NiS surface itself has a catalytic effect on  $\text{NH}_3$  production. The difference between the  $\text{NH}_3$  production rates of the  $\text{N}_2$  and Ar experiments for TU-NiS ( $52 \pm 5.57 \mu\text{g h}^{-1} \text{cm}^{-2}$ , depicted as  $\text{N}_2 - \text{Ar}$  in Fig. 2i) is much higher than the  $\text{NH}_3$  production rates of SS-NiS ( $1.45 \mu\text{g h}^{-1} \text{cm}^{-2}$ ) and B-NiS ( $6.78 \pm 0.68 \mu\text{g h}^{-1} \text{cm}^{-2}$ ), which indicates that TU (or TU-derived thiocyanate) acts as a promoter for NRR on the NiS surface. These results indicate that the TU-derived functional groups (e.g., thiocyanate) on the catalyst surface not only act as an N source but also contribute to boosting the NRR performance. We also note that the total  $\text{NH}_3$  yield ( $86.91 \pm 9.29 \mu\text{g h}^{-1} \text{cm}^{-2}$ ) estimated from the colorimetric assay is similar to the total  $\text{NH}_3$  yield ( $80.55 \mu\text{g h}^{-1} \text{cm}^{-2}$ ) estimated from the  $^1\text{H}$  NMR, while the difference between the  $\text{NH}_3$  yield from TU-NiS in the  $\text{N}_2$  environment and the  $\text{NH}_3$  yield from

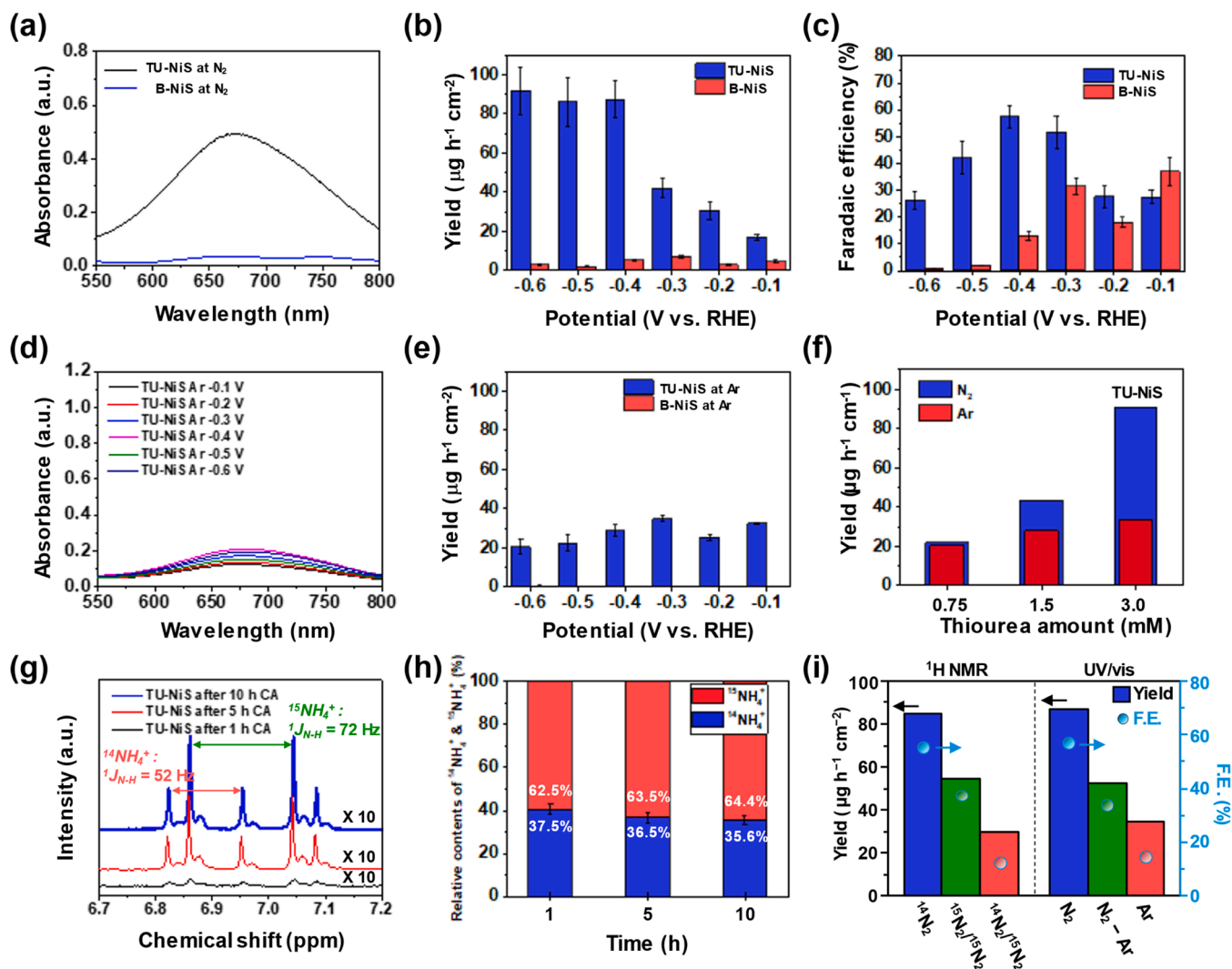


**Fig. 2.** (a) UV–vis absorption spectra for TU-NiS and B-NiS catalysts. (b)  $\text{NH}_3$  yield rates and (c) the corresponding F.E. for TU-NiS and B-NiS. (d) UV–vis absorption spectra for TU-NiS in a Ar environment and (e)  $\text{NH}_3$  yield rates for TU-NiS and B-NiS in a Ar environment. (f)  $\text{NH}_3$  yield and F.E. for the TU-NiS catalyst. For  $^1\text{H}$  NMR, integrated peaks under  $^{14}\text{N}_2$  feed ( $^{14}\text{N}_2$ ), integrated  $^{15}\text{N}_2$  peaks under  $^{15}\text{N}_2$  feed ( $^{15}\text{N}_2/^{15}\text{N}_2$ ), and integrated  $^{14}\text{N}_2$  peaks under  $^{15}\text{N}_2$  feed ( $^{14}\text{N}_2/^{15}\text{N}_2$ ) is presented. For UV/vis, results from  $\text{N}_2$  feed ( $\text{N}_2$ ), difference between the results of  $\text{N}_2$  feed and Ar feed ( $\text{N}_2 - \text{Ar}$ ), and results from Ar feed (Ar) is presented.

TU-NiS in the Ar environment ( $52 \pm 5.57 \mu\text{g h}^{-1} \text{cm}^{-2}$ ) is nearly identical to the  $^{15}\text{NH}_3$  yield from the  $^1\text{H}$  NMR results ( $50.37 \pm 1.67 \mu\text{g h}^{-1} \text{cm}^{-2}$ ). These results clearly show that  $^{14}\text{NH}_3$  from  $^1\text{H}$  NMR is produced by the reduction of internal N sources in catalysts such as surface thiocyanates, as the  $^{14}\text{NH}_3$  yield is very similar to the  $\text{NH}_3$  yield from TU-NiS in an Ar environment.

To further prove the catalytic effect of TU derived surface residues, we modified the surfaces of SS-NiS and B-NiS to have surface thiocyanate (SCN) residues and tested the NRR activity. The surface modification processes were performed to create thiocyanate residues on the surface of SS-NiS and B-NiS, and achieved by modifying the existing synthesis method. FT-IR analysis was performed to identify the peaks related to S–C≡N stretching, N–H bending and C–N stretching (Fig. S18). As a result, the peak at  $2170 \text{ cm}^{-1}$  can be assigned to the S–C≡N stretching vibration. Also, the peak at  $1608 \text{ cm}^{-1}$  is corresponded to N–H bending vibration. Finally, the peak at  $1234 \text{ cm}^{-1}$  is corresponded to C–N stretching vibration. Moreover, element analysis was used to confirm the amounts of C, N, and S contained in the samples, summarized in Table S2. Interestingly, both TU-B-NiS and TU-SS-NiS follow the same trend with TU-NiS, showing non-negligible amount of

$\text{NH}_3$  yield under Ar feed, yet the  $\text{NH}_3$  yield is significantly enhanced under  $\text{N}_2$  feed (Fig. S19). In contrast, pristine B-NiS and SS-NiS exhibited low  $\text{NH}_3$  yield under  $\text{N}_2$  feed and trace amounts of  $\text{NH}_3$  yield under Ar feed, clearly showing the effect of TU treatment.

The catalytic performance of the TU-NiS catalyst is compared with other reported metal sulfide electrocatalysts (Table S3), which shows that the ammonia yield of TU-NiS excluding thiocyanate reduction is larger than or comparable to other metal sulfide catalysts, while among the metal sulfide catalysts, TU-NiS exhibits superior F.E.

We also conducted long term stability test and cyclability tests for the TU-NiS catalyst (Fig. 3). The current density in the  $i$ - $t$  curve measured with CA for the TU-NiS catalyst under an  $\text{N}_2$  environment at  $U = -0.4 \text{ V}$  (vs. RHE) remained stable up to 12 h, and the current density was further stabilized from 20 h after a gradual change up to 20 h (Fig. 3a). We also measured the  $\text{NH}_3$  yield of the TU-NiS catalyst under  $\text{N}_2$  feed for 2 h intervals up to 10 h, and 10 h intervals from 10 h to 50 h and compared it to the same long-term test under Ar feed (Fig. 3b). In the  $\text{N}_2$  feed long-term test, the  $\text{NH}_3$  yield slowly saturates to the point where 42 % of the  $\text{N}_2 - \text{Ar}$  yield is maintained ( $24 \mu\text{g h}^{-1} \text{cm}^{-2}$  at the 50 h mark), compared to the 10 h mark around  $57 \mu\text{g h}^{-1} \text{cm}^{-2}$ . Most importantly,

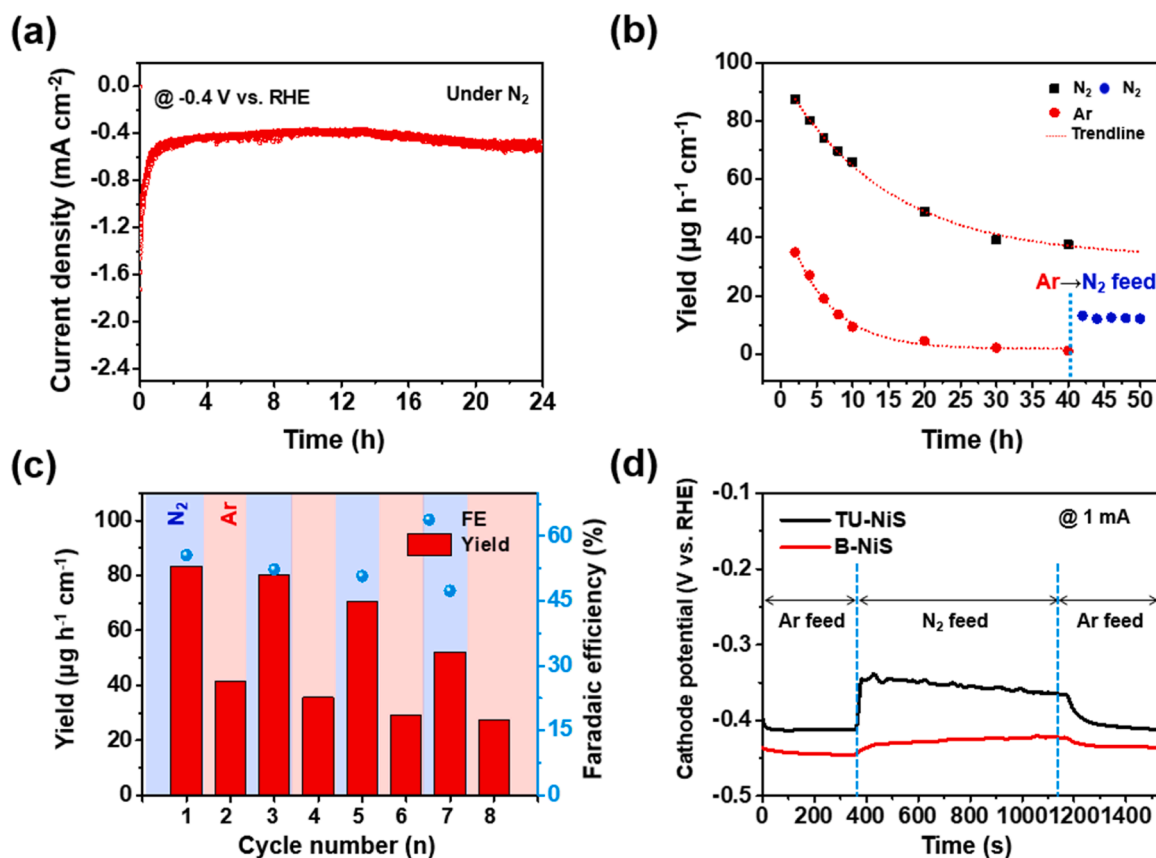


**Fig. 3.** Long term stability and cyclability test for the TU-NiS catalyst. (a) CA result of TU-NiS under an  $N_2$  environment for 24 h at  $U = -0.4$  V. (b)  $NH_3$  yield rates of TU-NiS under  $N_2$  environment and Ar environment for 40 h switching to  $N_2$  environment for 42, 44, 46, 48, and 50 h  $U = -0.4$  V. The red curve is presented for guidance. (c) Cycling stability for TU-NiS.  $NH_3$  yield and F.E. is represented for the cycle of repeated switching between  $N_2$  feeding conditions (blue background) and Ar feeding conditions (red background). Each cycle is conducted for 1 h at  $U = -0.4$  V. (d) CP results at 1 mA/cm $^2$  for TU-NiS and B-NiS catalysts with consecutive switching from Ar to  $N_2$  feeding and  $N_2$  to Ar feeding conditions.

the estimated amount of produced ammonia is 85.54  $\mu mol$  at the 12 h mark, which exceeds the total amount of  $NH_3$  that can be produced on internal N atoms of the TU-NiS (79.93  $\mu mol$  on an 88 mg of electrode evaluated from element analysis) assuming every single N atom is converted into  $NH_3$  in a 100 % rate. This provides solid evidence that  $NH_3$  is not solely from TU or SCN reduction and a significant amount of  $NH_3$  is produced from the catalytic NRR. On the other hand, in the same test under an Ar environment instead of  $N_2$ , the  $NH_3$  yield greatly decreases over time dropping down to a marginal value of 0.17  $\mu g h^{-1} cm^{-2}$  (Fig. 3b). Surprisingly, the  $NH_3$  yield increases to a nonnegligible value of 11.65  $\mu g h^{-1} cm^{-2}$  when switching the Ar gas feed to  $N_2$  gas feed after the 34 h of Ar experiment. The decrease in  $NH_3$  yield under Ar feed is additional proof of  $NH_3$  production by internal N sources, the surface thiocyanates, of the TU-NiS catalyst, while the increase of  $NH_3$  yield switching to  $N_2$  feed from Ar feed is further evidence of (reduced) thiocyanate acting as a NRR promoter. In addition, the significant decrease in the  $NH_3$  yield of the Ar-to- $N_2$  feed experiment suggests that the NRR active sites can be deactivated during the Ar feed experiment. This is proved by the  $N_2$ -Ar feed switching cyclability test (Fig. 3c). Here, the  $NH_3$  yield gradually decreases with the number of cycles, and up to 6 cycles, the  $NH_3$  yield difference between the  $N_2$  cycle and the following Ar cycle remains nearly constant (41.91, 44.54, 41.46  $\mu g h^{-1} cm^{-2}$  for the 1st-2nd cycle, 3rd-4th cycle, and the 5th-6th cycle, respectively) and comparable to the estimated  $NH_3$  yield of TU-NiS excluding  $NH_3$  from thiocyanate reduction (47.83  $\mu g h^{-1} cm^{-2}$ ). The abrupt  $NH_3$  yield decrease in the 7th  $N_2$  cycle suggests the NRR active sites are deactivated during the repeated cycles.

To explain the cause of catalyst deactivation, we compare the SEM, XRD, EDS (Fig. S20), and X-ray photoelectron spectroscopy (XPS) results between the as-prepared (Fig. S8) and 10 h post-NRR TU-NiS catalysts (Fig. S21). The overall crystal structure remains mostly the same (Fig. S20a-c), while the surface N and C contents significantly decrease after the NRR experiment due to the reduction of surface thiocyanate (Fig. S20d). Elemental analysis was carried out to clearly confirm the ratio and amount of C and N contained in the TU-NiS catalyst per unit mass. Elemental analysis confirmed that 1 g of TU-NiS catalysts contains 0.9925 mmol of N and 0.7016 mmol of C. Based on the aforementioned FT-IR and Raman analysis results, assuming that thiocyanate and a small amount of thiourea are adsorbed, it can be calculated that 1 g of TU-NiS catalysts contains 0.4107 mmol of thiocyanate (Fig. S20d).

After the NRR treatment, the XPS peak intensity for the S 2p region (Fig. S21a) is significantly reduced and there is no sign of SCN-related peaks, indicating most of the surface thiourea is reduced to ammonia and S atoms are degraded from the catalyst surface. The evolution of peaks from oxidized S species ( $SO_x^{2-}$ ) strongly indicate the possibility of S degradation via  $SO_x^{2-}$  ion dissolution. For the Ni 2p, C 1s, and N 1s spectra (Fig. S21b-d), new peaks evolved for the post-NRR TU-NiS catalyst surface, where we assign the peaks to Ni-C binding related peaks.

We also performed a chronopotentiometry (CP) test on the TU-NiS and B-NiS catalyst starting from an Ar environment, switching to an  $N_2$  environment and switching back to Ar feed (Fig. 3d). For the TU-NiS catalyst, a dramatic change in the cathode potential is observed when switching the feed gas between Ar and  $N_2$ , while the potential change is marginal for B-NiS. This clearly indicates the ammonia synthesis

mechanism in  $N_2$  feed is distinctive from the mechanism in Ar feed and  $N_2$  feed for the TU-NiS catalyst.

As mentioned earlier, NiS is predicted to be NRR active but was found to be even more active for the HER in another theoretical work [25]. To overcome this selectivity issue, we adopted cationic HER suppression [27–29] and NRR promotion effects [30] by optimizing the cation used for the electrolyte (Fig. S22). Among the electrolytes,  $Na_2SO_4$  shows the best performance for both  $NH_3$  yield and F.E. It has been reported the most optimal size for the cation depends on the cation adsorption on the catalyst surface [28,29], which indicates  $Na^+$  has the most optimal size for HER suppression for TU-NiS.

### 3.3. Catalytic mechanism of NRR on NiS catalysts

To gain insight into the catalytic NRR process on the TU-NiS surface and determine how thiocyanate acts as a promoter, we performed a mechanistic study using DFT (Fig. 3). It is revealed that Mars-van Krevelen-like mechanisms on the TU-NiS catalyst (Fig. S23) [54,55] and the associative NRR pathway [56,57] on pristine  $\alpha$ -NiS (001) and  $\beta$ -NiS (110) surfaces were both not feasible as the  $N_2$  molecular binding mostly form physisorption structures (Fig. S24) and no stable structures were found for the following protonation step of each configuration ( $*N_2 \rightarrow *N_2H$ ).

Here, we suggest an alternative reaction pathway initiated by thiocyanate reduction on the TU-NiS surface. After reduction of the cyanate group on the surface TU, the remaining C atom binds to a Ni atom and a S atom (Fig. 4a). A Bader charge analysis shows that the S atom binding with the remnant C atom is highly electron deficient (missing  $0.6e^-$  in

comparison to the substituted S atom in the pristine NiS) and, thus, is highly reactive and easily detachable from the surface. This result is consistent with the severe XPS intensity decrease of the S 1s spectra for the post-NRR TU-NiS (Fig. S21a). The deprivation of S leads to a highly reactive C site on the surface, which enables relatively facile  $N_2$  adsorption ( $E_{ads} = -0.4$  eV,  $G_{ads} = +0.1$  eV) on the active C site, which explains why Ni-C related peaks occur in the post-NRR TU-NiS XPS spectra (Fig. S21b-d). It has been reported hydrated cations from the electrolyte prohibits the protonation on catalyst surface by cation-cation repulsion [27–29]. To confirm whether cationic suppression can prohibit the protonation of the  $C^*$  site, we calculated the reaction barrier for the  $C^*$  site protonation reaction with a Na ion adsorbed on the surface (Fig. S25). The calculated reaction barrier for the proton transfer reaction is prohibitively high (0.97 eV) and the reaction free energy is marginal ( $E_{ads} = -0.2$  eV,  $G_{ads} = 0.0$  eV). Furthermore, we show the  $*H$  and  $*N_2$  adsorption energy difference between the pristine  $*C$  site and  $*C + Na$  site (Fig. S26). For  $*H$ , the adsorption energy is greatly destabilized with presence of the Na ion ( $G_{ads} = -1.1$  eV without Na,  $\rightarrow G_{ads} = 0.0$  eV with Na), clearly showing that surface adsorbed Na ion sufficiently suppressed the protonation of the  $*C$  site of the TU-NiS. On the other hand, the change in  $*N_2$  adsorption energy is marginal ( $G_{ads} = +0.1$  eV without Na,  $\rightarrow G_{ads} = +0.1$  eV with Na) due to the neutral and non-polar nature of the  $N_2$  molecule. This result clearly shows that the  $C^*$  site protonation is sufficiently suppressed, thus the NRR on the  $C^*$  site is not hindered by the HER, due to the prohibitive reaction barrier. In case of other sites, protonation on the S site on the TU-NiS surface ( $G_{ads} = +0.3$  eV) is more unstable than  $C^*$  even without Na suppression so we also rule out S site protonation. Neutral  $N_2$  gas

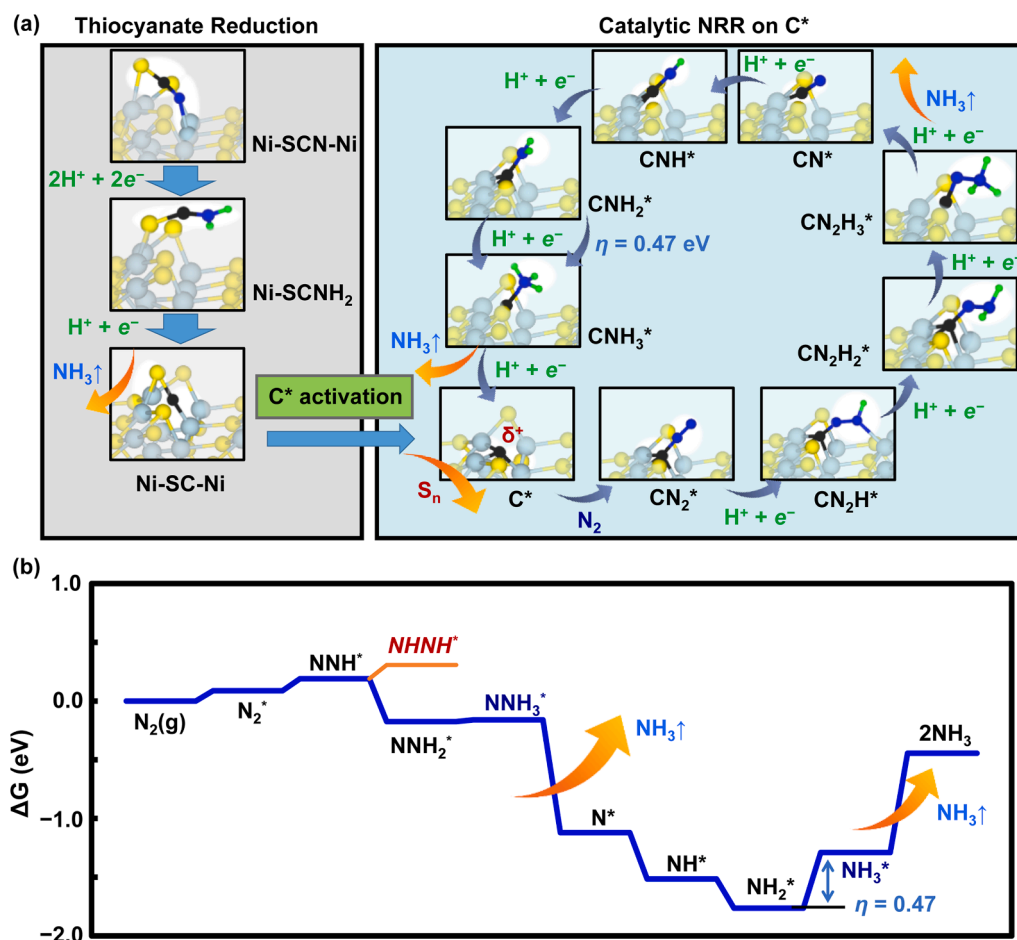


**Fig. 4.** (a) Schematic diagram of the total ammonia synthesis pathway on the TU-NiS surface. (b) Free energy diagrams of the NRR pathway on the TU-NiS surface at  $U = 0$  V. The PDS and  $\eta$  are depicted in eV. The color coding for the elements is as follows: Ni = light cyan, S = yellow, C = black, N = cobalt blue, and H = green.



molecules doesn't experience such repulsion and the protonation of  $\text{N}_2^*$  is relatively facile due to the distance between the protonation site and the catalyst surface [27–29]. The consecutive  $6e^-$  reduction of  $^*\text{N}_2$  to  $2\text{NH}_3$  under the distal mechanism [58,59] is feasible with  $\eta = 0.47$  V, where the rate-determining step (RDS) is the  $^*\text{NH}_3$  desorption step with  $\Delta G = 0.85$  eV (Fig. 4b). The reaction free energy change for the alternating mechanism [58,59] is higher than that for the distal mechanism by  $+0.48$  eV, where the difference is even higher than the limiting potential. As a result, the NRR on TU-NiS is expected to experience thiocyanate reduction, followed by the desorption of a neighboring S, and finally, nitrogen reduction under a distal mechanism on an active C site to produce  $\text{NH}_3$  (Fig. 4a). The two different ammonia synthesis mechanisms of surface cyanate reduction followed by the active-C-derived NRR explains the distinctive electrochemical behavior of Ar-feed and  $\text{N}_2$ -feed TU-NiS experiments.

Notably, the TU-reduction-derived catalytic C site is identical to a carbon substituting a S atom on the NiS surface. Since C has fewer valence electrons than S, this 'substitution' generates a very reactive catalytic C site. TU is a typical sulfur source for metal sulfide synthesis, especially for  $\text{MoS}_2$  synthesis. We investigated the possibility that the NRR mechanism is based on the TU-reduction-derived active carbon on  $\text{MoS}_2$  materials with DFT (Fig. S27). Our results show that the activated carbon indeed promotes the NRR for  $\text{MoS}_2$  by lowering the  $\text{N}_2$  adsorption free energy. As mentioned before, the catalytic C site can be regarded as a nonmetal dopant with fewer valence electrons than the nonmetal elements in metal-nonmetal compounds (e.g., metal sulfides, oxides, nitrides, etc.). Our results show the possibility of nonmetal dopants with fewer valence electrons acting as a reactive catalytic site for the NRR, providing another explanation for the NRR activities of reported catalysts such as C-doped  $\text{TiO}$  [60], C-doped BN [61],  $\text{NbTiO}_4/\text{N}$ -doped carbon hybrids [62], and MXene [63].

#### 4. Conclusions

In summary, we demonstrated that TU, a sulfur source typically used in metal sulfide synthesis, can provide false positives to the electrochemical NRR by enabling the reduction of TU-derived surface adsorbates such as thiocyanates. At the same time, the electrochemical reduction of the thiocyanates generates reactive C sites on the catalyst surfaces and paradoxically promotes the NRR performance after TU reduction, as proven by careful examination with various control experiments,  $^{15}\text{N}_2$  isotope experiments, and DFT calculations. Because the resulting catalytic C sites are similar to C substitution from a S atom on metal sulfide surfaces, this study opens possibilities for exploring metal-nonmetal compounds by nonmetal dopants with fewer valence electrons as NRR catalysts, such as C/P/N-doped chalcogenides, C-doped nitrides and phosphides. This study also shows that surface adsorbates can serve as promoters in NRR catalysts, which can lead to further enhancement of NRR performance by surface modification of the catalysts.

#### CRedit authorship contribution statement

**Min-Cheol Kim:** Conceptualization, Methodology, Formal analysis, Investigation, Writing - original draft, Visualization, and Funding acquisition. **Jiyong Chung:** Conceptualization, Methodology, Formal analysis, Investigation, Writing - original draft. **Tae-Yong An:** Methodology, Formal analysis, Investigation, Writing - original draft, Visualization. **Jaeyoung Lee:** Methodology, Formal analysis, Investigation, Writing - original writing, Visualization. **Mi-Kyung Han:** Investigation. **Shinbi Lee:** Investigation. **Wonyong Choi:** Investigation. **Jung Kyu Kim:** Formal Analysis. **Sang Soo Han:** Writing - review & editing, Project administration, Funding acquisition. **Uk Sim:** Writing - review & editing, Project administration, Funding acquisition. **Taekyung Yu:** Writing - review & editing, Project administration, Funding acquisition.

#### Declaration of Competing Interest

The authors declare that they have no known competing financial interests or personal relationships that could have appeared to influence the work reported in this paper.

#### Data availability

Data will be made available on request.

#### Acknowledgements

This work was supported by the Creative Materials Discovery Program through the National Research Foundation of Korea (NRF-2016M3D1A1021141) and the National Center for Materials Research Data (NCMRD) through the National Research Foundation of Korea funded by the Ministry of Science and ICT (2021M3A7C2089739). M.-C. K. acknowledges the support by the National Supercomputing Center with supercomputing resources including technical support (KSC-2022-CRE-0027) and the support by Basic Science Research Program through the National Research Foundation of Korea (NRF) funded by the Ministry of Education (2022R111A1A01064152). T.Y. acknowledges financial support from the National Research Foundation of Korea (NRF) grants funded by the Korean government (MSIP) (NRF-2021R1A5A6002853 and NRF-2020R1A2C1003885).

#### Appendix A. Supporting information

Supplementary data associated with this article can be found in the online version at doi:10.1016/j.apcatb.2023.122485.

#### References

- [1] J.W. Erisman, M.A. Sutton, J. Galloway, Z. Klimont, W. Winiwarter, How a century of ammonia synthesis changed the world, *Nat. Geosci.* 1 (2008) 636–639.
- [2] S. Giddey, S.P.S. Badwal, C. Munnings, M. Dolan, Ammonia as a renewable energy transportation media, *ACS Sustain. Chem. Eng.* 5 (2017) 10231–10239.
- [3] J. Guo, P. Chen, Catalyst:  $\text{NH}_3$  as an energy carrier, *Chem* 3 (2017) 709–712.
- [4] T.H. Rod, A. Logadottir, J.K. Nørskov, Ammonia synthesis at low temperatures, *J. Chem. Phys.* 112 (2000) 5343–5347.
- [5] J.-H. Zhou, Y.-W. Zhang, Metal-based heterogeneous electrocatalysts for reduction of carbon dioxide and nitrogen: mechanisms, recent advances and perspective, *React. Chem. Eng.* 3 (2018) 591–625.
- [6] J.G. Chen, R.M. Crooks, L.C. Seefeldt, K.L. Bren, R.M. Bullock, M.Y. Darensbourg, P.L. Holland, B. Hoffman, M.J. Janik, A.K. Jones, M.G. Kanatzidis, P. King, K. M. Lancaster, S.V. Lymar, P. Pfromm, W.F. Schneider, R.R. Schrock, Beyond fossil fuel-driven nitrogen transformations, *Science* 360 (2018) eaar6611.
- [7] S.L. Foster, S.L.P. Bakovic, R.D. Duda, S. Maheshwari, R.D. Milton, S.D. Minter, M. J. Janik, J.N. Renner, L.F. Greenlee, Catalysts for nitrogen reduction to ammonia, *Nat. Catal.* 1 (2018) 490–500.
- [8] L. Wang, M. Xia, H. Wang, K. Huang, C. Qian, C.T. Maravelias, G.A. Ozin, Greening ammonia toward the solar ammonia refinery, *Joule* 2 (2018) 1055–1074.
- [9] B.H.R. Suryanto, H.-L. Du, D. Wang, J. Chen, A.N. Simonov, D.R. MacFarlane, Challenges and prospects in the catalysis of electroreduction of nitrogen to ammonia, *Nat. Catal.* 2 (2019) 290–296.
- [10] X. Li, G. Hai, J. Liu, F. Zhao, Z. Peng, H. Liu, M.K.H. Leung, H. Wang, Bio-inspired  $\text{NiCoP}/\text{CoMoP}/\text{Co}(\text{Mo}_3\text{Se}_4)_4$  @C/NF multi-heterojunction nanoflowers: effective catalytic nitrogen reduction by driving electron transfer, *Appl. Catal. B-Environ.* 314 (2022), 121531.
- [11] W. Liang, W. Qin, D. Li, Y. Wang, W. Guo, Y. Bi, Y. Sun, L. Jiang, Localized surface plasmon resonance enhanced electrochemical nitrogen reduction reaction, *Appl. Catal. B-Environ.* 301 (2022), 120808.
- [12] Z. Liu, T. Huang, H. Chang, F. Wang, J. Wen, H. Sun, M. Hossain, Q. Xie, Y. Zhao, Y. Wu, Computational design of single Mo atom anchored defective boron phosphide monolayer as a high-performance electrocatalyst for the nitrogen reduction reaction, *Energy Environ. Mater.* 4 (2021) 255–262.
- [13] B.K. Burgess, D.J. Lowe, Mechanism of molybdenum nitrogenase, *Chem. Rev.* 96 (1996) 2983–3012.
- [14] S. Raugel, L.C. Seefeldt, B.M. Hoffman, Critical computational analysis illuminates the reductive-elimination mechanism that activates nitrogenase for  $\text{N}_2$  reduction, *Proc. Natl. Acad. Sci.* 115 (2018) E10521–E10530.
- [15] X. Chen, Y.-T. Liu, C. Ma, J. Yu, B. Ding, Self-organized growth of flower-like  $\text{SnS}_2$  and forest-like  $\text{ZnS}$  nanoarrays on nickel foam for synergistic superiority in electrochemical ammonia synthesis, *J. Mater. Chem. A* 7 (2019) 22235–22241.
- [16] D. Feng, X. Zhang, Y. Sun, T. Ma, Surface-defective  $\text{FeS}_2$  for electrochemical  $\text{NH}_3$  production under ambient conditions, *Nano Mater. Sci.* (2019).



- [17] Y. Guo, Z. Yao, B.J.J. Timmer, X. Sheng, L. Fan, Y. Li, F. Zhang, L. Sun, Boosting nitrogen reduction reaction by bio-inspired FeMoS containing hybrid electrocatalyst over a wide pH range, *Nano Energy* 62 (2019) 282–288.
- [18] M.-C. Kim, H. Nam, J. Choi, H.S. Kim, H.W. Lee, D. Kim, J. Kong, S.S. Han, S.Y. Lee, H.S. Park, Hydrogen bonding-mediated enhancement of bioinspired electrochemical nitrogen reduction on Cu<sub>2</sub>-S catalysts, *ACS Catal.* 10 (2020) 10577–10584.
- [19] M. Lashgari, P. Zeinalkhani, Ammonia photosynthesis under ambient conditions using an efficient nanostructured FeS<sub>2</sub>/CNT solar-energy-material with water feedstock and nitrogen gas, *Nano Energy* 48 (2018) 361–368.
- [20] X. Li, X. Ren, X. Liu, J. Zhao, X. Sun, Y. Zhang, X. Kuang, T. Yan, Q. Wei, D. Wu, A. MoS<sub>2</sub> nanosheet-reduced graphene oxide hybrid: an efficient electrocatalyst for electrocatalytic N<sub>2</sub> reduction to NH<sub>3</sub> under ambient conditions, *J. Mater. Chem. A* 7 (2019) 2524–2528.
- [21] Y.-T. Liu, X. Chen, J. Yu, B. Ding, Carbon-nanoplated CoS@TiO<sub>2</sub> nanofibrous membrane: an interface-engineered heterojunction for high-efficiency electrocatalytic nitrogen reduction, *Angew. Chem. Int. Ed.* 58 (2019) 18903–18907.
- [22] D. Zhang, Y. Liu, B. Mao, H. Li, T. Jiang, D. Zhang, W. Dong, W. Shi, Double-phase heterostructure within Fe-doped Cu<sub>2</sub>-S quantum dots with boosted electrocatalytic nitrogen reduction, *ACS Sustain. Chem. Eng.* 9 (2021) 2844–2853.
- [23] L. Li, W. Yu, W. Gong, H. Wang, C.-L. Chiang, Y. Lin, J. Zhao, L. Zhang, J.-M. Lee, G. Zou, Sulfur-induced electron redistribution of single molybdenum atoms promotes nitrogen electroreduction to ammonia, *Appl. Catal. B-Environ.* 321 (2023), 122038.
- [24] J. Wen, H. Sun, Q. Zhou, Z. Liu, T. Huang, X. Chen, X. Yang, Q. Huang, Y. Chen, Y. Wu, One-step hydrothermal synthesis of Co–Ni–S/Ni foam as an electrocatalyst for nitrogen reduction reaction, *Mater. Today Energy* 26 (2022), 100995.
- [25] Y. Abghoui, S.B. Sigtrygsson, E. Skúlason, Biomimetic nitrogen fixation catalyzed by transition metal sulfide surfaces in an electrolytic cell, *ChemSusChem* 12 (2019) 4265–4273.
- [26] X. Chen, J. Liu, T. Yuan, Z. Zhang, C. Song, S. Yang, X. Gao, N. Wang, L. Cui, Recent advances in earth-abundant first-row transition metal (Fe, Co and Ni)-based electrocatalysts for the oxygen evolution reaction, *Energy Mater.* 2 (2022), 200028.
- [27] Y.-C. Hao, Y. Guo, L.-W. Chen, M. Shu, X.-Y. Wang, T.-A. Bu, W.-Y. Gao, N. Zhang, X. Su, X. Feng, J.-W. Zhou, B. Wang, C.-W. Hu, A.-X. Yin, R. Si, Y.-W. Zhang, C.-H. Yan, Promoting nitrogen electroreduction to ammonia with bismuth nanocrystals and potassium cations in water, *Nat. Catal.* 2 (2019) 448–456.
- [28] L. Ou, H. Zhou, Theoretical insights into the origin of promoter effect of alkali metals on Au-catalyzed nitrogen electroreduction, *Chem. Phys. Lett.* 789 (2022), 139320.
- [29] N.C. Kani, A. Prajapati, B.A. Collins, J.D. Goodpaster, M.R. Singh, Competing effects of pH, cation identity, H<sub>2</sub>O saturation, and N<sub>2</sub> concentration on the activity and selectivity of electrochemical reduction of N<sub>2</sub> to NH<sub>3</sub> on electrodeposited Cu at ambient conditions, *ACS Catal.* 10 (2020) 14592–14603.
- [30] N.C. Kani, A. Prajapati, B.A. Collins, J.D. Goodpaster, M.R. Singh, Competing effects of pH, cation identity, H<sub>2</sub>O saturation, and N<sub>2</sub> concentration on the activity and selectivity of electrochemical reduction of N<sub>2</sub> to NH<sub>3</sub> on electrodeposited Cu at ambient conditions, *ACS Catal.* 10 (2020) 14592–14603.
- [31] J. Choi, B.H.R. Suryanto, D. Wang, H.-L. Du, R.Y. Hodgetts, F.M. Ferrero Vallana, D.R. MacFarlane, A.N. Simonov, Identification and elimination of false positives in electrochemical nitrogen reduction studies, *Nat. Comm.* 11 (2020) 5546.
- [32] G. Kresse, J. Furthmüller, Efficiency of ab-initio total energy calculations for metals and semiconductors using a plane-wave basis set, *Comput. Mater. Sci.* 6 (1996) 15–50.
- [33] B. Hammer, L.B. Hansen, J.K. Nørskov, Improved adsorption energetics within density-functional theory using revised Perdew-Burke-Ernzerhof functionals, *Phys. Rev. B* 59 (1999) 7413–7421.
- [34] S. Grimme, J. Antony, S. Ehrlich, H. Krieg, A consistent and accurate ab initio parametrization of density functional dispersion correction (DFT-D) for the 94 elements H–Pu, *J. Chem. Phys.* 132 (2010), 154104.
- [35] G. Kresse, D. Joubert, From ultrasoft pseudopotentials to the projector augmented-wave method, *Phys. Rev. B* 59 (1999) 1758–1775.
- [36] T. Bögels, Analyzing HER catalytic sites of nickel sulphides, a DFT computational study, *Dep. Earth Sci. -Geochem., Utrecht Univ.* (2019).
- [37] J.K. Nørskov, J. Rossmeisl, A. Logadottir, L. Lindqvist, J.R. Kitchin, T. Bligaard, H. Jónsson, Origin of the overpotential for oxygen reduction at a fuel-cell cathode, *J. Phys. Chem. B* 108 (2004) 17886–17892.
- [38] NIST. N.I.S.T. chemistry webbook, 2018.
- [39] K. Mathew, R. Sundaraman, K. Letchworth-Weaver, T.A. Arias, R.G. Hennig, Implicit solvation model for density-functional study of nanocrystal surfaces and reaction pathways, *J. Chem. Phys.* 140 (2014), 084106.
- [40] D. Sheppard, R. Terrell, G. Henkelman, Optimization methods for finding minimum energy paths, *J. Chem. Phys.* 128 (2008), 134106.
- [41] Z.D. Wang, M. Yoshida, B. George, Theoretical study on the thermal decomposition of thiourea, *Comput. Theor. Chem.* 1017 (2013) 91–98.
- [42] C.-Z. Zhang, M.-X. Niu, Study on mechanism of isomerization between ammonium thiocyanate and thiourea, *J. Mol. Struct.* 1125 (2016) 643–648.
- [43] G. Rahman, S.Y. Chae, O.-s. Joo, Efficient hydrogen evolution performance of phase-pure NiS electrocatalysts grown on fluorine-doped tin oxide-coated glass by facile chemical bath deposition, *Int. J. Hydrogen Energy* 43 (2018) 13022–13031.
- [44] A.R. Pratt, H.W. Nesbitt, Core level electron binding energies of realgar (As<sub>4</sub>S<sub>4</sub>), *Am. Mineral.* 85 (2000) 619–622.
- [45] Z. Yang, M. Wang, J. Ding, Z. Sun, L. Li, J. Huang, J. Liu, J. Shao, Semi-transparent ZnO-CuI/CuSCN photodiode detector with narrow-band UV photoresponse, *ACS Appl. Mater. Interfaces* 7 (2015) 21235–21244.
- [46] N. Chandra Deb Nath, K. Yoo, J.-J. Lee, Halogen-free guanidinium-based perovskite solar cell with enhanced stability, *RSC Adv.* 8 (2018) 17365–17372.
- [47] D.R. Mullins, D.R. Huntley, S.H. Overbury, The nature of the sulfur induced surface reconstruction on Ni(111), *Surf. Sci.* 323 (1995) L287–L292.
- [48] NIST. NIST X-ray Photoelectron Spectroscopy Database, NIST Standard Reference Database Number 20, 2000.
- [49] M.-H. Vu, M. Sakar, C.-C. Nguyen, T.-O. Do, Chemically bonded Ni cocatalyst onto the S Doped G-C<sub>3</sub>N<sub>4</sub> nanosheets and their synergistic enhancement in H<sub>2</sub> production under sunlight irradiation, *ACS Sustain. Chem. Eng.* 6 (2018) 4194–4203.
- [50] M. Shalom, D. Ressnig, X. Yang, G. Clavel, T.P. Feller, M. Antonietti, Nickel nitride as an efficient electrocatalyst for water splitting, *J. Mater. Chem. A* 3 (2015) 8171–8177.
- [51] P.S. Bagus, E.S. Ilton, C.J. Nelin, The interpretation of XPS spectra: Insights into materials properties, *Surf. Sci. Rep.* 68 (2013) 273–304.
- [52] S.-Y. Lo, W. Dianbudiyanto, S.-H. Liu, Selective recovery of platinum from spent autocatalyst solution by thiourea modified magnetic biocarbons, *Sci. Rep.* 11 (2021) 19281.
- [53] E. Murray, E.P. Nesterenko, M. McCaul, A. Morrin, D. Diamond, B. Moore, A colorimetric method for use within portable test kits for nitrate determination in various water matrices, *Anal. Methods* 9 (2017) 680–687.
- [54] X. Yang, J. Nash, J. Anibal, M. Dunwell, S. Kattel, E. Stavitski, K. Attenkofer, J. G. Chen, Y. Yan, B. Xu, Mechanistic insights into electrochemical nitrogen reduction reaction on vanadium nitride nanoparticles, *J. Am. Chem. Soc.* 140 (2018) 13387–13391.
- [55] X. Yang, S. Kattel, J. Nash, X. Chang, J.H. Lee, Y. Yan, J.G. Chen, B. Xu, Quantification of active sites and elucidation of the reaction mechanism of the electrochemical nitrogen reduction reaction on vanadium nitride, *Angew. Chem. Int. Ed.* 58 (2019) 13768–13772.
- [56] E. Skúlason, T. Bligaard, S. Gudmundsdóttir, F. Studt, J. Rossmeisl, F. Abild-Pedersen, T. Vegge, H. Jónsson, J.K. Nørskov, A theoretical evaluation of possible transition metal electro-catalysts for N<sub>2</sub> reduction, *Phys. Chem. Chem. Phys.* 14 (2012) 1235–1245.
- [57] J.H. Montoya, C. Tsai, A. Vojvodic, J.K. Nørskov, The challenge of electrochemical ammonia synthesis: a new perspective on the role of nitrogen scaling relations, *ChemSusChem* 8 (2015) 2180–2186.
- [58] X. Guo, J. Gu, X. Hu, S. Zhang, Z. Chen, S. Huang, Coordination tailoring towards efficient single-atom catalysts for N<sub>2</sub> fixation: A case study of iron-nitrogen-carbon (Fe@N-C) systems, *Catal. Today* (2019).
- [59] L. Xia, J. Yang, H. Wang, R. Zhao, H. Chen, W. Fang, A.M. Asiri, F. Xie, G. Cui, X. Sun, Sulfur-doped graphene for efficient electrocatalytic N<sub>2</sub>-to-NH<sub>3</sub> fixation, *Chem. Comm.* 55 (2019) 3371–3374.
- [60] Q. Qin, Y. Zhao, M. Schmalleger, T. Heil, J. Schmidt, R. Walczak, G. Gescheidt-Demmer, H. Jiao, M. Oschatz, Enhanced electrocatalytic N<sub>2</sub> reduction via partial anion substitution in titanium oxide–carbon composites, *Angew. Chem. Int. Ed.* 58 (2019) 13101–13106.
- [61] C. Ma, Y. Zhang, S. Yan, B. Liu, Carbon-doped boron nitride nanosheets: a high-efficient electrocatalyst for ambient nitrogen reduction, *Appl. Catal. B-Environ.* 315 (2022), 121574.
- [62] D.K. Yesudoss, H. Chun, B. Han, S. Shanmugam, Accelerated N<sub>2</sub> reduction kinetics in hybrid interfaces of NbTiO<sub>4</sub> and nitrogen-doped carbon nanorod via synergistic electronic coupling effect, *Appl. Catal. B-Environ.* 304 (2022), 120938.
- [63] Y. Luo, G.-F. Chen, L. Ding, X. Chen, L.-X. Ding, H. Wang, Efficient electrocatalytic N<sub>2</sub> fixation with MXene under ambient conditions, *Joule* 3 (2019) 279–289.